

# Enhancing the Electrocatalytic Activity of Redox Stable Perovskite Fuel Electrodes in Solid Oxide Cells by Atomic Layer Deposited Pt Nanoparticles

Arunkumar Pandiyan<sup>1§</sup>, Valerio Di Palma<sup>2§</sup>, Vasileios Kyriakou<sup>1,3,\*</sup>, Wilhelmus M. M. Kessels<sup>2</sup>, Mariadriana Creatore<sup>2</sup>, Mauritijs C. M. van de Sanden<sup>1,2</sup>, Mihalis N. Tsampas<sup>1,\*</sup>

<sup>1</sup>*DIFFER is the Dutch Institute For Fundamental Energy Research, De Zaale 20, 5612 AJ, Eindhoven, the Netherlands*

<sup>2</sup>*Department of Applied Physics, Eindhoven University of Technology, 5600 MB Eindhoven, the Netherlands*

<sup>3</sup>*Department of Nuclear Science and Engineering, Massachusetts Institute of Technology, 77 Massachusetts Avenue, Cambridge, MA 02139, USA*

*§First and second authors have contributed equally and possess the first authorship of this article.*

**\*Corresponding authors:** [kyriakou@mit.edu](mailto:kyriakou@mit.edu), [m.tsampas@diff.nl](mailto:m.tsampas@diff.nl)

## ABSTRACT

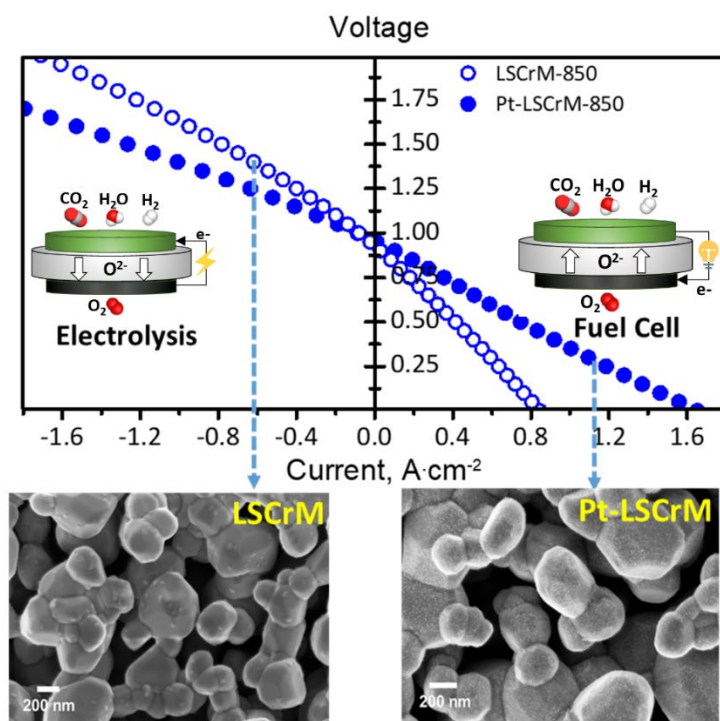
The carbon dioxide and steam co-electrolysis in solid oxide cells offers an efficient way to store the intermittent renewable electricity in the form of syngas (CO+H<sub>2</sub>), which constitutes a key intermediate for chemical industry. The co-electrolysis process, however, is challenging in terms of materials selection. The cell composites, and particularly the fuel electrode, is required to exhibit adequate stability in redox environments and coking that rules out the conventional Ni cermets. La<sub>0.75</sub>Sr<sub>0.25</sub>Cr<sub>0.5</sub>Mn<sub>0.5</sub>O<sub>3</sub> (LSCrM) perovskite oxides represents a promising alternative solution, but with electrocatalytic activity inferior to the conventional Ni-based cermets. Here we report on how the electrochemical properties of a state-of-the-art LSCrM electrode can be significantly enhanced by introducing uniformly distributed Pt nanoparticles (18 nm) on its surface via the atomic layer deposition (ALD). At 850 °C, Pt nanoparticle deposition resulted in a ~62% increase of the syngas production rate during electrolysis mode (at 1.5 V), whereas the power output was

improved by ~84% at fuel cell mode. Our results exemplify how the powerful ALD approach can be employed to uniformly disperse small amounts ( $\sim 50 \mu\text{g}\cdot\text{cm}^{-2}$ ) of highly active metals to boost the limited electrocatalytic properties of redox stable perovskite fuel electrodes with efficient material utilization.

## KEYWORDS

syngas production; atomic layer deposition; CO<sub>2</sub> reduction; H<sub>2</sub>O electrolysis; greenhouse gases; solid oxide cells; Pt catalyst

## GRAPHICAL ABSTRACT



## SYNOPSIS

ALD deposited Pt nanoparticles for boosting  $\text{CO}_2\text{-H}_2\text{O}$  co-electrolysis towards the efficient conversion of greenhouse gases and renewable electricity into raw material for chemicals

## INTRODUCTION

Rapid greenhouse gas emissions from fossil fuels is the primary source of global warming, which escalates the shift towards eco-friendly fuel matrix powered by renewable energy.<sup>1</sup> Producing renewable electricity from solar and wind resources is intermittent, and thus, effective systems for storing the energy for continuous supply is required. The use of renewable energy for the production of synthetic fuels might be an efficient solution for a sustainable future, since the investments required to modify the existing infrastructure are avoided and carbon dioxide emissions could be stabilized.<sup>2-4</sup> In particular, solid oxide electrolysis cells (SOECs) have been drawing more attention as a viable system to convert CO<sub>2</sub> and H<sub>2</sub>O, at adequate reaction rates, into syngas (CO+H<sub>2</sub>) which is a key intermediate for the synthetic fuel production via Fischer Tropsch reaction.<sup>4-6</sup>

The traditional SOECs adopt identical materials to the solid oxide fuel cells (SOFCs) that primarily involve a Ni-based cermet as the fuel electrode (cathode), yttria-stabilized zirconia (YSZ) as the electrolyte and (La,Sr)MnO<sub>3</sub> perovskites for the oxygen electrode (anode). The Ni-YSZ cathode in SOEC, however, is exposed to a variable oxygen partial pressure environment and thus, is ultimately decaying due to the coarsening of the Ni particles.<sup>7,8</sup> To restrain Ni oxidation a reducing agent, such as H<sub>2</sub> or CO, is co-introduced to the cathode atmosphere, hence increasing process' cost and complexity.<sup>5,9</sup>

In view of this, redox stable perovskites (ABO<sub>3</sub>) materials with mixed ionic-electronic conducting properties (MIEC) have been examined as the cathodic electrodes in SOECs. Specifically, lanthanum chromates, such as La<sub>1-x</sub>Sr<sub>x</sub>Cr<sub>1-y</sub>Mn<sub>y</sub>O<sub>3-δ</sub> (LSCrM), constitute a class of perovskites which exhibit MIEC properties and redox stability, combined with an adequate tolerance to CO<sub>2</sub>

as compared to the traditional nickel-based electrodes.<sup>10-13</sup> Under the direct electrolysis of CO<sub>2</sub>, the LSCrM based fuel electrode has been well-adapted, but the performance of the cathode is limited by higher polarization resistance and limited catalytic activity than Ni-based cermet.<sup>14</sup> The p-type conductivity of LSCrM (38 S cm<sup>-1</sup> at  $pO_2 > 10^{-10}$  atm) drastically declines under reducing bias due to the reduction of Cr<sup>4+</sup>/Mn<sup>4+</sup> to Cr<sup>3+</sup>/Mn<sup>3</sup> in parallel with the development of oxygen vacancies.<sup>15,16</sup> Hence, the LSCrM exhibits higher ionic conductivity, whereas its electrical conductivity significantly decreases at reducing atmospheres. To date, the outright performance of LSCrM for co-electrolysis has not still reached the performance of Ni-based cermets.<sup>5,17</sup>

To enhance electrochemical properties of the perovskites, the introduction of catalytically active metal nanoparticles onto the surface of the electrodes has been widely employed.<sup>5,17</sup> The most common routes for preparing these nanostructures are the infiltration and exsolution processes. Both methods have been proven to significantly decrease the polarization resistance and increase the catalytic properties of the fuel electrode.<sup>18,19</sup> Nevertheless, the above techniques display important drawbacks which still hold back upscale. Infiltration is a rather poor technique in terms of reproducibility, requiring a number of intermediate steps while there is not sufficient control over the particle size and distribution.<sup>20</sup> For, examples infiltration process of Pt particle in La<sub>0.2</sub>Sr<sub>0.25</sub>Ca<sub>0.45</sub>TiO<sub>3</sub> electrode results in a bimodal distribution of larger particle size ranging between 100-150 nm.<sup>21</sup> By exsolution, on the other hand, unique and stable architectures of uniformly distributed nanoparticles can be formed.<sup>6,22</sup> The active phase, however, should be doped in the solid solution of the oxide support, thus decreasing the degrees of freedom in the electrode design. Moreover, during exsolution only a small part of the active phase is released upon reduction, which increases the fabrication cost of the cell, particularly in the case noble metals.<sup>23,24</sup>

Regarding the macroporous structure of cathode with high surface area, atomic layer deposition (ALD) can be a valid alternative to decorate the macroporous structure of the cathode by Pt nanoparticles. ALD is a deposition method based on the cyclic dosing of vapor-phase species reacting with the substrate in a self-limiting fashion. ALD is commonly adopted for the preparation of thin films, albeit the deposition of metals is characterized by the nucleation of small islands in the initial stages of the process.<sup>25</sup> This characteristic feature can be applied to prepare metallic nanoparticles for catalysis.<sup>26</sup> Due to the self-limiting nature of the reactions, ALD allows for digital control over the amount of metal deposited.<sup>27,28</sup> Furthermore, it is also suitable for deposition on the porous and 3D-complex substrate on which it can result in well-dispersed nanoparticles with high conformality on surface features and high reproducibility.<sup>29-31</sup> ALD works related to the modification of SOFC electrode have been already reported in literature to tune the electrochemical activity of oxygen electrode but not for the fuel electrode.<sup>32,33,34</sup> The high control over the metal loading also allows to vary the coverage area of the surface, and thus, the exposed area of underlying perovskite to the gas-solid interface, which in turn is crucial for O<sup>2-</sup> species exchange during the co-electrolysis process. Moreover, ALD has the potential to make compatible atomic-scale precision with industrial-scale production,<sup>27</sup> for which the control over the amount of Pt deposited is an advantage in view of the cost reduction. Therefore, ALD provides a potential solution to overcome the engineering issue associated with the deposition of metal nanoparticles on porous perovskite-based electrodes in order to improve their electrocatalytic properties.

Here we report on ALD as an alternative method to infiltration for boosting the electrochemical properties of LSCrM by introducing Pt nanoparticles onto the fuel electrode's surface. Platinum increases mass/charge transfer exchange rate, and simultaneously is among the optimum catalysts towards H<sub>2</sub>O/CO<sub>2</sub> electrolysis.<sup>21,35</sup> Pt was one of the extensively studied metal catalyst for

promoting the reverse water-gas-shift (RWGS) reaction to produce syngas.<sup>36,37</sup> Further, in case of perovskite supported catalyst (lanthanum doped zirconate), Pt reported to show increased CO<sub>2</sub> conversion in electrically assisted RWGS as compared to Ni, Cu, Fe, Pd.<sup>38</sup> Hence, by combining the well-distributed Pt nanoparticles with the high number of oxygen vacancies of LSCrM an active interface for CO<sub>2</sub> and H<sub>2</sub>O reduction is generated, enhancing the efficiency for syngas production. Our studies demonstrate how ALD can be a powerful tool for fabricating unique nanoarchitectures in solid oxide cells in order to transform low reactivity but abundant molecules to chemical feedstock and store the intermittent renewable electricity into chemical bonds.

## EXPERIMENTAL

### *Material Synthesis*

The LSCrM electrode of a La<sub>0.75</sub>Sr<sub>0.25</sub>Cr<sub>0.5</sub>Mn<sub>0.5</sub>O<sub>3</sub> stoichiometry was synthesized via the citric-acid combustion process by using lanthanum(III) nitrate hexahydrate (La(NO<sub>3</sub>)<sub>3</sub>·6H<sub>2</sub>O, Sigma-Aldrich, 99.99%), strontium nitrate (Sr(NO<sub>3</sub>)<sub>2</sub>, Sigma-Aldrich, 99.99%), chromium(III) nitrate nonahydrate (Cr(NO<sub>3</sub>)<sub>3</sub>·9H<sub>2</sub>O, Sigma-Aldrich, 9.99%) and manganese(II) nitrate hydrate (Mn(NO<sub>3</sub>)<sub>2</sub>·H<sub>2</sub>O, Sigma-Aldrich, 98%) precursors. The stoichiometric amount of nitrates (oxidizer) required was dissolved in deionized water, followed by the addition of citric acid (fuel), with metal to fuel mole ratio of 1:1.5. Ammonium hydroxide was added to adjust the pH value between 6 and 7. The transparent gel formed after drying the solution at 80°C for 12 h was then ignited at 300 °C on a hot plate. The powder obtained after the combustions process was calcined at 700 °C for 2 h, followed by sintering at 1100 °C for 2 h.

### *Cell Preparation*

The electrochemical performance was evaluated using an electrolyte-supported button-like single cell with a configuration of LSCrM (10 $\mu$ m)/GDC(8 $\mu$ m)|ScCeSZ (150 $\mu$ m)|LSM-YSZ (8 $\mu$ m)/LSM (8 $\mu$ m) were fabricated using a screen-printing method. The ScCeSZ (150  $\mu$ m thickness) electrolyte used in the study was commercially purchased from Fuel cell Materials. Gadolinium (10 mol%) doped cerium oxide (GDC) was screen printed over electrolyte and fired at 1300 °C for 4 h, acting as a buffer layer between the electrolyte and fuel electrode to improve the adhesion with the polished ScCeSZ solid electrolyte.<sup>22</sup> The fuel electrode of LSCrM was screen printed over the GDC buffer layer and dried at 80 °C. Thereafter, the oxygen electrode screen printing was carried out using lanthanum strontium manganite (LSM), and Ytria stabilized zirconia (YSZ) from fuel cell materials. The complete cell was fired at 1100 °C for 2 h in the air with the heating and cooling rate of 2.5 °C/min. Au paint and mesh was used as a current collector during electrochemical studies.

### *ALD of Pt*

Platinum was deposited into the porous LSCrM fuel electrode by ALD using a home-built reactor, already described in the literature.<sup>40,41</sup> The pumping system, consisting of a turbopump connected to a rotary pump, enabled to keep the base pressure of the reactor < 10<sup>-6</sup> mbar. The walls of the chamber were heated to 90 °C while the substrate holder was heated to 300 °C. Trimethyl(methylcyclopentadienyl)platinum(IV) (MeCpPtMe<sub>3</sub>, 98% purity) purchased from Sigma-Aldrich was used as precursor for the process. MeCpPtMe<sub>3</sub> was contained in a stainless steel cylindrical bubbler heated to 30 °C. Argon gas (> 99.999% purity) was used to carry

MeCpPtMe<sub>3</sub> vapor from the bubbler to the reactor through a line heated to 50 °C. O<sub>2</sub> gas (> 99.999% purity) used as a reactant was flowed at the pressure of 1.0 mbar.

The ALD process used was based on the work of *Aaltonen et al.*<sup>42</sup> first to report ALD of Pt using MeCpPtMe<sub>3</sub> and oxygen. The ALD recipe selected was based on our previous work<sup>31</sup> in which an LSM-GDC substrate was decorated with well dispersed Pt NPs. The recipe starts by flowing Ar, in order to stabilize the pressure inside the chamber to  $2.0 \cdot 10^{-2}$  mbar and then dosing MeCpPtMe<sub>3</sub> for 4 s by diverting Ar through the bubbler. Subsequently, Ar is flowed for 3 s to purge the precursor line, and the reactor is pumped down for 3 s. Afterward, O<sub>2</sub> gas is dosed for 10 s, and then the reactor is pumped down for 10 s.

#### *Pt loading*

In order to determine the loading of Pt after ALD, three samples have been prepared and weighted using a Microbalance Cubis MSE 6.6S-000-DM (Sartorius). The average weight for each sample has been determined on 9 measurements. ALD has been performed on two substrates for the determination of the Pt loading. A bare LSCrM substrate and one Pt/LSCrM substrate have been exposed to 850 °C for 4 h for the determination of any weight difference.

#### *Electrochemical characterization*

The electrochemical studies were carried out on the homemade solid oxide cell reactor with heat and gas flow controller. Alumina based cement (Cotronics) was used to seal the cell between the anode and cathode chamber. I-V (current-voltage) curves and EIS (electrochemical impedance spectra) measurements were carried out using a potentiostat (CompactStat, Ivium Technologies) operating at 800 °C and 850 °C. EIS analysis was performed at the OCV within the frequency range of 1 Mhz – 1hZ with 20 mV amplitude. The flow of CO<sub>2</sub>, H<sub>2</sub>, and air were precisely

controlled by the mass flow controllers (Brooks), followed by mixing with the water vapor using a controlled heating saturator. The gas line from the humidifier to the reactor in the furnace was maintained at 120 °C to avoid the steam condensation. The gas analysis was performed using an online infra-red analyzer (Fuji Electric) and micro gas chromatograph (SRA Instruments).

### *Material Characterization*

The crystallographic phase analysis was studied using X-ray powder diffractometer (Bruker) with monochromatic Cu K $\alpha$  incident radiation produced at 40KV, 25 mA to the diffraction angles ( $2\theta$ ) between 20° - 90° with a step size of 0.02°/s. Rietveld refinement of powder XRD pattern was performed using FullProf software package. Vesta was used to visualize the 3D crystal structure of a refined XRD pattern. To gain insights on the chemical composition of the electrode at the surface, X-ray photoemission spectroscopy (XPS) studies were carried out on a Thermo Scientific K-Alpha system, equipped with a monochromatic Al K $\alpha$  x-ray source at 1486.6 eV. To study the morphology of the electrodes, scanning electron microscopy (SEM) images were obtained with a Supra 40 (Carl Zeiss AG) microscope using an in-lens detector and accelerating voltage between 3 kV and 4 kV. For the determination of the particle size distribution from the SEM images the software ImageJ was used.

## RESULTS AND DISCUSSION

### *Characterization*

The phase analysis of the as-synthesized LSCrM system was determined through room temperature X-ray diffraction (XRD) and the results are presented in Figure 1a. The observed XRD peaks are in good agreement with the standard ICDD card nos. 01-070-8669 confirming the characteristic diffraction pattern of the perovskite phase. The Rietveld refinement of LSCrM patterns revealed a single-phase crystal structure of rhombohedral symmetry with  $R-3c$  space group with no detectable secondary phases or impurities. The XPS spectra depicts the chemical composition of the pristine LSCrM electrode (Figure 1b (red line) & Figure S1), confirming the synthesis of the La, Sr, Cr, and Mn mixed oxide. The presence of Pt on the perovskite surface following ALD is verified by the peaks at 71 eV and 315 eV characteristic of the Pt4f and Pt4d energy levels, respectively (Figure 1b (blue line), Figure S2-S3). The SEM images in Figures 1c and 1d display the morphology of the LSCrM electrode prior and following ALD process, respectively. It can be observed that the smoother granular structure of the electrode is uniformly decorated with Pt nanoparticles after the ALD process.

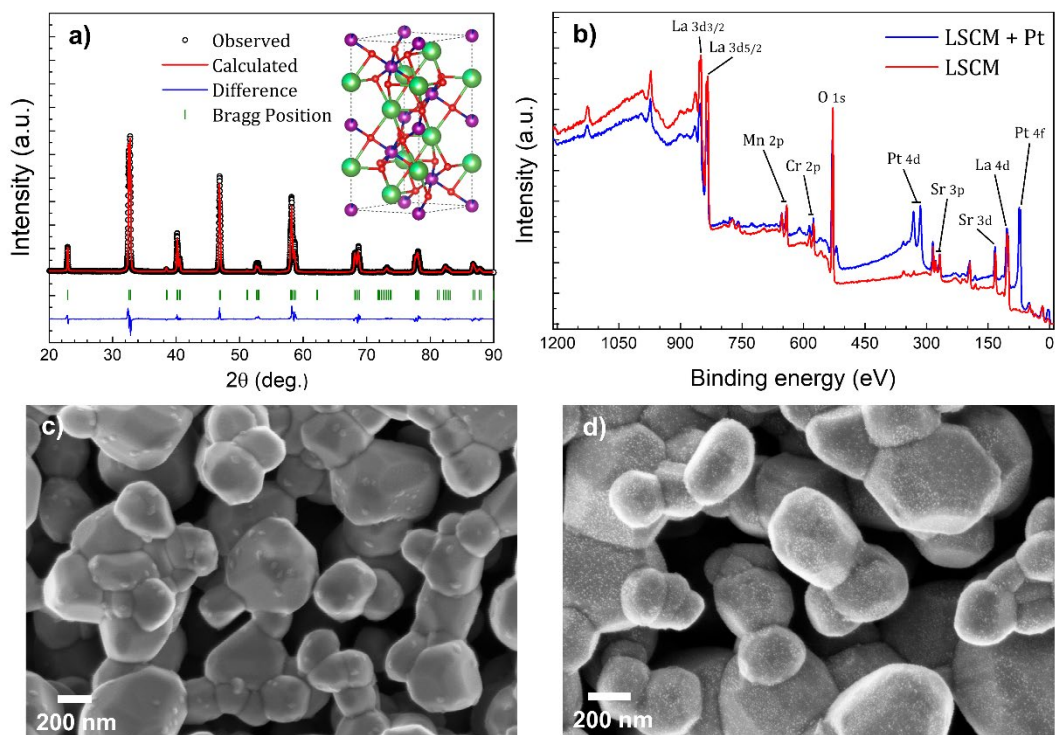


**Figure 1:** a) XRD diffractogram and refined pattern of LSCrM electrode material sintered at 1100 °C for 2 h. b) XPS survey of LSCrM substrate (red line) and LSCrM after Pt deposition (blue line); SEM top view image of the LSCrM substrate c) before and d) after Pt deposition.

The ALD process used has been demonstrating good reproducibility over time (see Figure S4). The number of ALD cycles has been selected to obtain a particle size well below the percolation threshold in order to expose a large surface area of the LSCrM to the gas feed. As matter of fact our previous report shows that 100 ALD cycles resulted in well dispersed Pt nanoparticles with average particle size of 6.5 nm<sup>31</sup>, therefore we selected the same number of cycles for the work reported hereby. Higher magnification SEM images (Figures 2a and 2b) have been acquired to determine the Pt particle size distribution (PSD) and the results are shown in Figures 2c and 2d. In the as-deposited case, the overall PSD histogram (Figure 2e) reveals an average particle size of 6.5

nm with a standard deviation of 1.6 nm. Interestingly those values are in line with our previous work where similar characteristics were observed for the metal nanoparticles.<sup>31</sup> The SEM images (Figures 2a, 2b, and Figure S5 in the Supplementary Information) depict a slightly different coverage of Pt in some areas of the LSCrM grains. That growth behavior is not unexpected since ALD growth of Pt nanoclusters can be affected by the chemical composition of the substrate due to the difference in surface energy but also in the surface kinetics of the process.<sup>43</sup>

The Pt nanoparticles in the as-deposited condition have been observed up to 4  $\mu\text{m}$  into the porous electrode (see Figure S6 in the Supplementary Information). Nevertheless we cannot exclude the presence, deeper into the porous electrode, of smaller Pt nanoparticles which would not be visible at the resolution of the SEM.

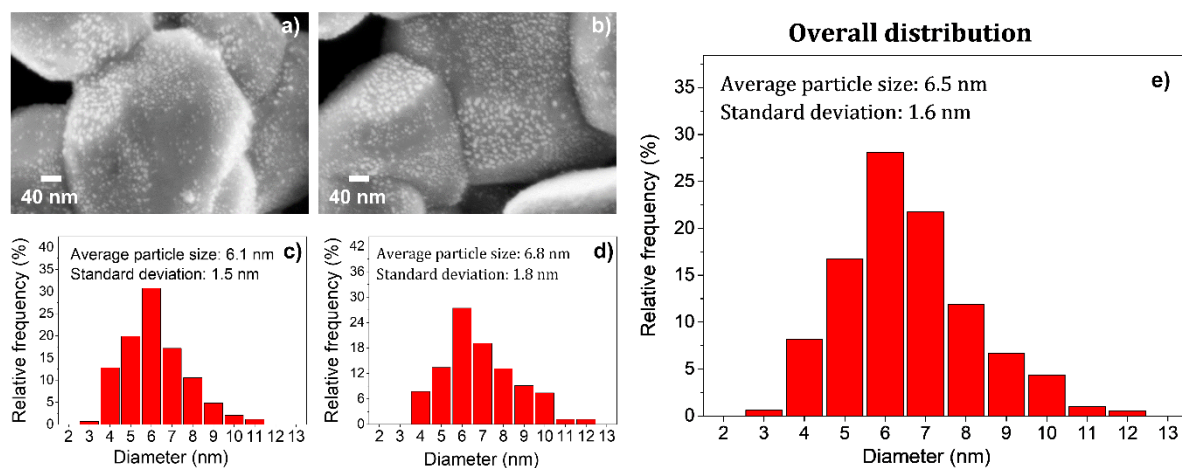


**Figure 2:** a), b) Higher magnification SEM images of the as-deposited Pt nanoparticles on LSCrM and c), d) respective particle size distribution. The overall distribution e) of the Pt nanoparticles has been determined in four different areas of the sample (see Figure S5 in the Supplementary Information).

By determining the Pt loading on LSCrM after the ALD (Tables S2 and S3 in the Supplementary Information) values of  $51 \pm 2 \mu\text{g}\cdot\text{cm}^{-2}$  and  $50 \pm 1 \mu\text{g}\cdot\text{cm}^{-2}$  on the two different samples are observed,

indicating the good homogeneity of the process. Moreover, we measured the weight of the Pt/LSCrM sample after exposure at high temperature (850 °C, 4 hr). The weight change observed was minor (from  $51 \pm 2 \mu\text{g}\cdot\text{cm}^{-2}$  to  $48 \pm 2 \mu\text{g}\cdot\text{cm}^{-2}$ ) implying that the loading of Pt is practically constant during the thermal treatment. It should be noted that obtaining similar loading values with other techniques is challenging. For instance with infiltration the weight range is between 0.2 and 2  $\text{mg}\cdot\text{cm}^{-2}$ , which is from 4 to 40 times higher than the results obtained by ALD in the present work.<sup>44,45</sup>

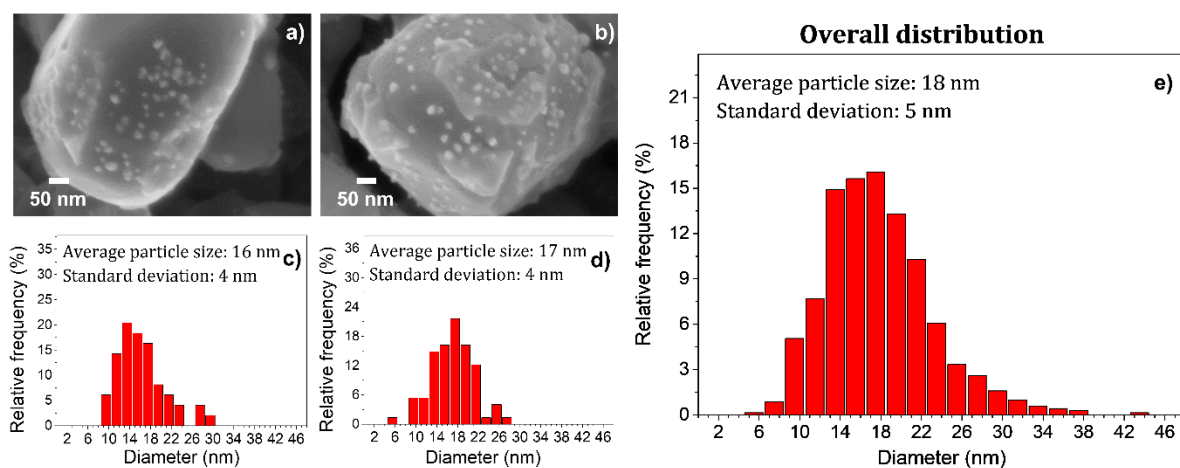


**Figure 3:** a), b) High magnification SEM images of the Pt nanoparticles on LSCrM exposed at high temperature (850 °C) and c), d) respective particle size distribution. The overall distribution after high-temperature exposure e) has been determined in four different areas of the sample (see Figure S7 in the Supplementary Information).

The changes in the morphology of the Pt/LSCrM electrode upon exposure to high temperature (850 °C, 4 hr) was studied by means of SEM (see Figure S7 in the Supplementary Information). This analysis was performed to evaluate what is the effective structure of the Pt nanoparticles under operational conditions. As expected, the SEM images display a lower particle coverage due

to a higher average size (Figures 3a and 3b) with respect to the pristine Pt-decorated LSCrM sample. The average particle size has increased to 18 nm with a standard deviation of 5 nm (Figure 3e). By assuming a constant Pt total volume, we can estimate the proportion between the number of particles prior and after heat treatment. A change in the diameter from 6.5 nm to 18 nm corresponds to a decrease of the number of particles by a factor of 21, i.e. about 21 particles of 6.5 nm are needed to make a particle of 18 nm after Pt agglomeration. This proportion justifies the emergence of low particle density areas at the substrate.

Additionally, the effect of heat treatment on the distribution of Pt into the open volume of the substrate has been addressed. Before exposure to high temperature, Pt nanoparticles were observed at the cross-section SEM to reach up to 4  $\mu\text{m}$  deep into the surface of the electrode (see Figure S6 in the Supplementary Information). After the heat treatment Pt nanoparticles seems to penetrate deeper into the porous structure, being visible from the top surface to the LSCrM-electrolyte interface (see Figure S8 in the Supplementary Information). A possible contribution to the appearance of Pt nanoparticles at the bottom of the electrode can also be given by the presence of smaller nanoparticles, not visible from SEM, that have been agglomerating upon annealing. Nevertheless, XPS surface analysis (Figure S9) of the electrode exhibits a strong decrease of the Pt 4f peak upon annealing, supporting the hypothesis of the diffusion of the particles from the top to the bottom of the electrode.

In all cases reported above, namely from the as-deposited sample to the heat-treated, the particle size distribution exhibits the right-skewed shape typical of Smoluchowski aggregation.<sup>46</sup> This suggests that both in the ALD process and in heat exposure, the growth mechanism of Pt nanoparticles is governed by the sintering via dynamic diffusion and coalescence.

### *Electrochemical activity*

Figure 4 illustrates the surface and the cross-sectional microstructure of the LSCrM/GDC/ScCeSZ/LSM-YSZ/LSM fabricated cell. The LSCrM fuel electrode exhibits a highly porous microstructure to facilitate gases diffusion with thickness close to  $\sim 10\mu\text{m}$ . The dense buffer layer of GDC depicts a thickness of around  $6-8\mu\text{m}$  after the sintering procedure. The cross-sectional SEM image of the LSM-YSZ/LSM oxygen electrode shows adequate adhesion with the electrolyte and it is also highly porous to facilitate gas diffusion.<sup>6</sup> The XRD analysis was performed on the cell before and after Pt deposition, which reflects the diffraction peaks corresponding to LSCrM, GDC and YSZ (Figure S10). However, the diffraction peaks belongs to Pt were not significant after ALD deposition. It can be explained by the ultra-low loading of Pt on LSCrM electrode, which not sensitive enough to reflect a Pt peak in the X-ray diffraction pattern.

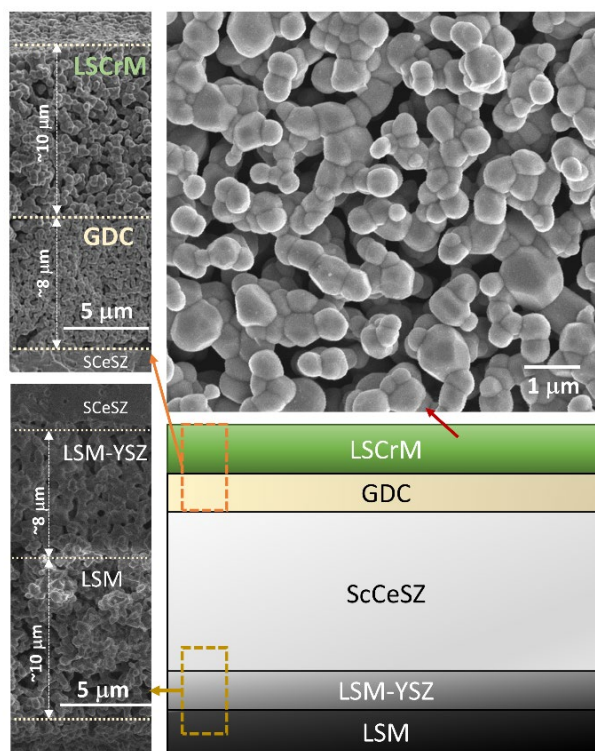


**Figure 4:** SEM surface morphology and structure of the fabricated cell.

Following fabrication, the cell was mounted on the testing reactor, and the Pt deposited LSCrM (Pt/LSCrM) fuel electrode was exposed to the synthetic air at 850 °C for 4 hrs. As expected, the Pt nanoparticles on the LSCrM electrode undergo agglomeration upon annealing, as shown in Figure 3 and Figures S7 and S8 in the Supplementary Information. The electrochemical experiments were carried out at 800 °C and 850 °C. The gas balance of mixture in all studies was adjusted using He as the carrier gas. In order to check the gas-tightness between two electrodes, H<sub>2</sub> and air were supplied to the anode and the cathode respectively, and the OCV measured was around ~1.0 V, which ensures the adequate sealing between the two chambers. The electrocatalytic performance of LSCrM and Pt/LSCrM were evaluated at both fuel cell and electrolysis modes of operation. The mixture of the feed gas for the fuel electrode was maintained at 25%H<sub>2</sub>O - 25%CO<sub>2</sub> - 50%H<sub>2</sub>, while the air was supplied to the oxygen electrode. The I-V characteristics and electrochemical impedance spectra (EIS) are recorded for the cells at different temperatures (800 °C and 850 °C) and shown in Figure 5.

The Nyquist plot of EIS data recorded at an open-circuit voltage (OCV) consists of two arcs with all samples at different temperatures. From the Nyquist plots, the contribution of Area Specific Resistance (ASR) of electrode polarization and ohmic resistance can be separated. The high-frequency intercept on the real axis represents the ohmic contribution from the electrolyte. The difference between low- and high-frequency intercept represent the polarization resistance (R<sub>p</sub>). Table 1 summarizes the obtained R<sub>p</sub> value derived from the EIS spectra at OCV. With the increase in temperature, both ohmic- and polarization-resistance decreases for electrolyte and electrode respectively, indicating the thermal activation process. Negligible change in ohmic resistance of cell with and without Pt was observed at a given temperature. On the other hand, the electrode polarization of cell with Pt deposited LSCrM was 2- and 1.5-times lower than the bare LSCrM

electrode at 800 °C and 850 °C, respectively at OCV. Further, the  $R_p$  value of Pt deposited LSCrM electrode ( $0.49 \Omega \cdot \text{cm}^2$ ) shows lesser values as compared to the Ni-YSZ cathode ( $0.69 \Omega \cdot \text{cm}^2$ )<sup>22</sup> in an identical operation/configuration condition. Thus the Pt/LSCrM electrode exhibits improved electrochemical performance as compared to the pristine LSCrM and standard Ni-YSZ cermet.

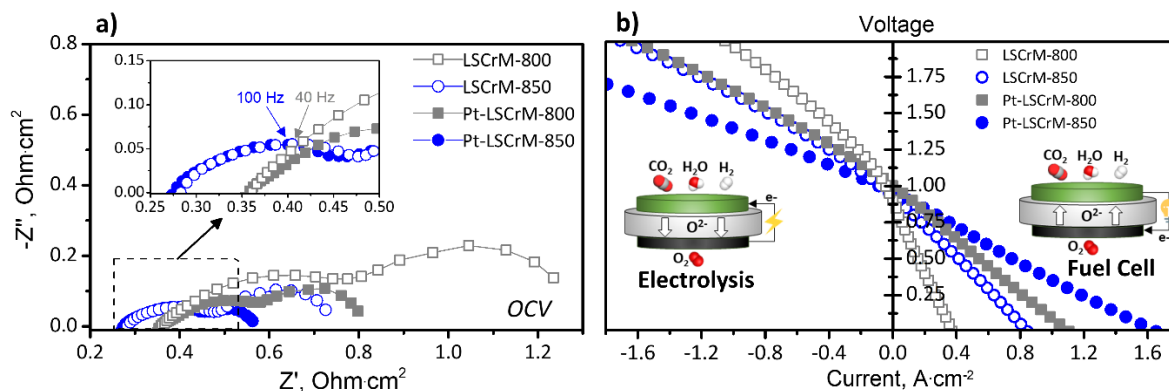


**Figure 5:** Electrochemical Performance of LSCrM with and without Pt deposition under reversible SOFC operation at 800 °C and 850 °C. (a) Nyquist plot and (b) I-V polarization curve for 25% $\text{H}_2\text{O}$ -25%  $\text{CO}_2$ -50% $\text{H}_2$  feed.

The I-V characteristics in Figure 5 show both positive and negative current indicating the power generation (SOFC) or consumption mode (SOEC), respectively. The I-V curve transit recorded at the scan rate of  $20 \text{ mV} \cdot \text{s}^{-1}$  displays a smooth transition between two operational modes demonstrates the good reversibility of the cell. In the SOFC region, the energy is generated by consuming the fuel (syngas), while in SOEC mode, the syngas is produced by consuming the electrical energy. In electrolysis mode (SOEC), at 1.5 V, the observed current densities of Pt/LSCrM cell are  $-0.73 \text{ A} \cdot \text{cm}^{-2}$  and  $-1.26 \text{ A} \cdot \text{cm}^{-2}$ , at 800 °C and 850 °C, respectively. In contrast, the bare LSCrM at 1.5 V exhibits a lower current density of  $-0.46 \text{ A} \cdot \text{cm}^{-2}$  and  $-0.78 \text{ A} \cdot \text{cm}^{-2}$  at 800 °C and 850 °C, respectively. Upon switching on the same device to the SOFC mode, the power

density ( $P = I \cdot V$ ) of Pt/LSCrM cell was up to  $270 \text{ mW} \cdot \text{cm}^{-2}$  and  $370 \text{ mW} \cdot \text{cm}^{-2}$  at  $800 \text{ }^\circ\text{C}$  and  $850 \text{ }^\circ\text{C}$ , respectively. The power outputs of the cell operating without the Pt nanoparticles was  $80 \text{ mW} \cdot \text{cm}^{-2}$  and  $201 \text{ mW} \cdot \text{cm}^{-2}$  at  $800 \text{ }^\circ\text{C}$  and  $850 \text{ }^\circ\text{C}$ , respectively.

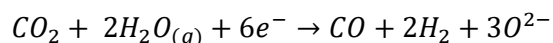
**Table 1:** Polarization resistance and total area specific resistance of LSCrM electrode with and without Pt deposition for the different temperature at  $800 \text{ }^\circ\text{C}$  and  $850 \text{ }^\circ\text{C}$ .

Fuel electrode	Temperature ( $^\circ\text{C}$ )	Polarization Resistance ( $R_p$ ) at OCV ( $\Omega \cdot \text{cm}^2$ )	Total Area Specific Resistance of Cell ( $\Omega \cdot \text{cm}^2$ )	
			at Fuel cell $I = 0.2 \text{ A/cm}^2$	at Electrolysis $I = -0.2 \text{ A/cm}^2$
LSCrM	800	0.97	2.31	1.81
	850	0.46	1.00	0.84
Pt-LSCrM	800	0.48	0.88	0.76
	850	0.30	0.50	0.49

In the co-electrolysis mode, in a similar configuration and operating conditions with electrolyte ( $150 \text{ } \mu\text{m}$ ) supported cell the Ni-YSZ cermet results in  $-0.63 \text{ A}$  at  $1.5 \text{ V}$ ,<sup>22</sup> which is 50% less than Pt/LSCrM electrode ( $-1.26 \text{ A}$  at  $1.5 \text{ V}$ ). Furthermore, in fuel cell mode, the Ni-YSZ based electrode reported to show  $300 \text{ mW cm}^{-2}$  at  $850^\circ\text{C}$ , while Pt/LSCrM in present work shows  $370 \text{ mW cm}^{-2}$ .<sup>22</sup> Also, our results are also comparable ( $\sim 10\text{-}20\%$  difference in current density) to the Ni-YSZ cermet supported cells where the electrolyte thickness did not exceed  $20 \text{ } \mu\text{m}$ .<sup>7,47-49</sup> Thus, Pt/LSCrM electrode demonstrates the high electrocatalytic performance as compare to the standard Ni-YSZ electrode.

The ASR value of the electrode for both electrolysis and fuel cell mode was derived from the I-V curve corresponding to  $\pm 0.2 \text{ A}\cdot\text{cm}^{-2}$  are reported in Table 1. The ASR value in fuel cell mode provides information about the activity of electrode on the usage of fuel to produce energy, i.e.  $\text{H}_2$  or/and CO (via Reverse Water Gas shift) oxidation to  $\text{H}_2\text{O}$  or/and  $\text{CO}_2$  respectively. On the other hand, the electrolysis ASR value depicts the electrode activity towards fuel generation ( $\text{H}_2$  and CO) by consuming the energy. The LSCrM electrode with Pt-deposition shows the lowest ASR value of  $0.49 \text{ }\Omega\cdot\text{cm}^{-2}$  at  $850 \text{ }^\circ\text{C}$  under co-electrolysis mode,  $0.35 \text{ }\Omega\cdot\text{cm}^{-2}$  lower than the bare LSCrM in the same condition. Similarly, at  $800 \text{ }^\circ\text{C}$ , the Pt/LSCrM electrode exhibits lower ASR value as compared to the bare LSCrM. The lower ASR value can be attributed to the enhancement of electrochemical performance for both fuel cell and electrolysis mode, indicating higher electrocatalytic activity and electrical conductivity compared to the cell without Pt.

To determine the syngas formation at the co-electrolysis operation, we performed a transient experiment at  $850 \text{ }^\circ\text{C}$  by applying different currents ( $0.2, 0.3, \text{ and } 0.6 \text{ A}\cdot\text{cm}^{-2}$ ), and the results have been reported in Figure 6. The experiments were carried out using  $25\%\text{H}_2\text{O} - 25\%\text{CO}_2 - 50\%\text{He}$  without co-feeding any reducing agent (as CO or  $\text{H}_2$ ). Under galvanostatic condition with constant removal of  $\text{O}^{2-}$  from the fuel electrode, the syngas generated as per the reaction as follows:



A stable potential of 1.1, 1.2, and 1.4 V seems to be attained for Pt/LSCrM at  $0.2, 0.3, \text{ and } 0.6 \text{ A}\cdot\text{cm}^{-2}$ , respectively. On the other hand, for bare LSCrM, the increase in potential was observed for the same applied current. Furthermore, I-R analyzer were used to measure the rate of  $\text{H}_2$  and CO production for the applied current of  $0.2, 0.3 \text{ and } 0.6 \text{ A}\cdot\text{cm}^{-2}$ . In both samples, the higher  $\text{H}_2$  production rate denotes the dominance of steam electrolysis. At  $0.6 \text{ A}\cdot\text{cm}^{-2}$ ,  $\text{H}_2$  attained

a maximum of 3.02 and 2.95 sccm·cm<sup>-2</sup>, while the CO production stays at a lower level of 1.33 and 1.21 sccm·cm<sup>-2</sup> for the samples with and without Pt, respectively.

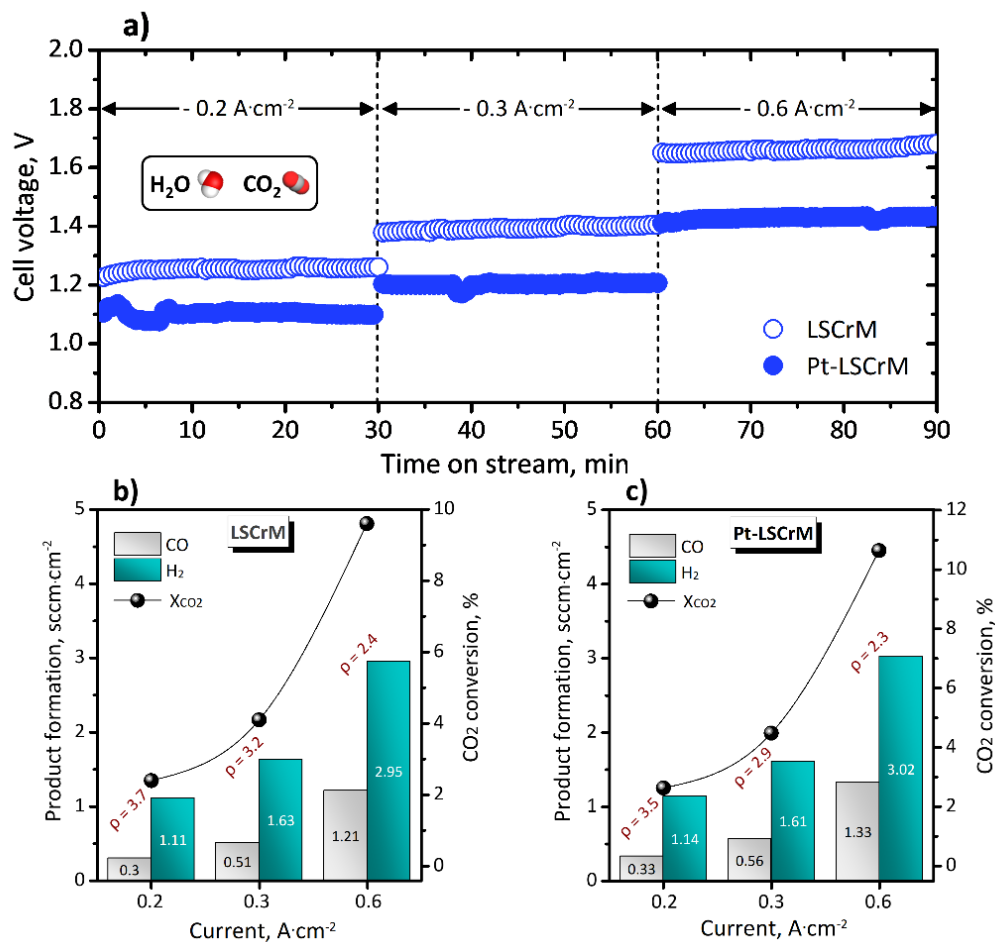


**Figure 6:** a) Effect of time on cell voltage transient during galvanostatic electrolysis of 25%H<sub>2</sub>O-25%CO<sub>2</sub> at 850 °C. b) and c) represent the corresponding syngas production rate with H<sub>2</sub>/CO ratio (ρ) during electrolysis of 25%H<sub>2</sub>O - 25%CO<sub>2</sub> - 50%He at 850 °C.

The steam and carbon dioxide co-electrolysis constitutes a more complexed system than the separate electrolysis processes. since CO can be generated both electrochemically from CO<sub>2</sub> (CO<sub>2</sub> + 2e<sup>-</sup> → CO + O<sup>2-</sup>) and catalytically via the reverse water gas shift reaction (RWGS) (CO<sub>2</sub> + H<sub>2</sub>

→ CO + H<sub>2</sub>O ,  $\Delta H^{\circ} = 41.2 \text{ kJ}\cdot\text{mol}^{-1}$ ).<sup>44-46</sup> The contribution of each route to CO production is still under debate in literature, strongly depending on the operational conditions but with most of the studies to agree that the catalytic route is the dominant route.<sup>48-50</sup> To gain further insight into CO formation, we conducted background studies for the individual H<sub>2</sub>O and CO<sub>2</sub> electrolysis over the Pt-LSCrM electrocatalyst (Figure S11). The attained current densities for the dry electroreduction of CO<sub>2</sub> were inferior to H<sub>2</sub>O and CO<sub>2</sub>-H<sub>2</sub>O co-electrolysis processes. Nevertheless, the faradaic efficiency to CO exceeded 90%, revealing that even though the direct CO<sub>2</sub> electroreduction is less favorable to H<sub>2</sub>O electrolysis, it should not be neglected from the CO formation.

The ratio between H<sub>2</sub>/CO ( $\rho$ ) constitutes an essential parameter of syngas regarding its further processing and suitability in industrial processes, in which a ratio between  $\rho = 1.0$  to  $3.0$  is usually preferred.<sup>51</sup> Here, the observed  $\rho$  values for the two electrodes examined was in the range of  $1.9$  to  $3.7$  (Figures 6b, 6c). Further, the  $\rho$  varied from  $2.3$  to  $3.5$  with the applied current (or voltage), revealing the advantage of using redox stable perovskites for the process which could offer a wide variety of syngas for several industrial applications from the same cell reactor.

#### *Durability Test:*

The short-term stability of the Pt/LSCrM fuel electrode was assessed by performing the co-electrolysis process for a period of 60 h at  $-0.2 \text{ A}$  and  $800 \text{ }^{\circ}\text{C}$  in  $25\%\text{H}_2\text{O} - 25\%\text{CO}_2 - 50\%\text{He}$ . The electrolysis voltage of the cell shows gradually increase in voltage from  $1.2$  to  $1.3 \text{ V}$  during 60 h of operation (Figure 7a). To understand this increase in voltage, SEM microstructural analysis on cross-section was carried out for the Pt/LSCrM electrode after 60 h of durability study (Figures 7b, 7c). The adhesion between the electrode and electrolyte interface seems to be unaltered during the study. Compared to the sample prior to the co-electrolysis experiments (heat-treated at  $850 \text{ }^{\circ}\text{C}$

for 4 h), the size of the Pt NPs on LSCrM backbone undergoes a negligible change after the durability test demonstrating the excellent stability of Pt NPs. The carbon nanofibers observed on the electrode after the stability test can possibly explain the increase in voltage. Also, the degradation will occur due to the contact loss between Au mesh and electrode at higher operating temperatures. Therefore, the carbon deposition and current collection issues contribute to the slight degradation during electrolysis, which constitutes no surprise since similar phenomena have been reported in solid oxide electrolysis studies.<sup>22,52,53</sup>

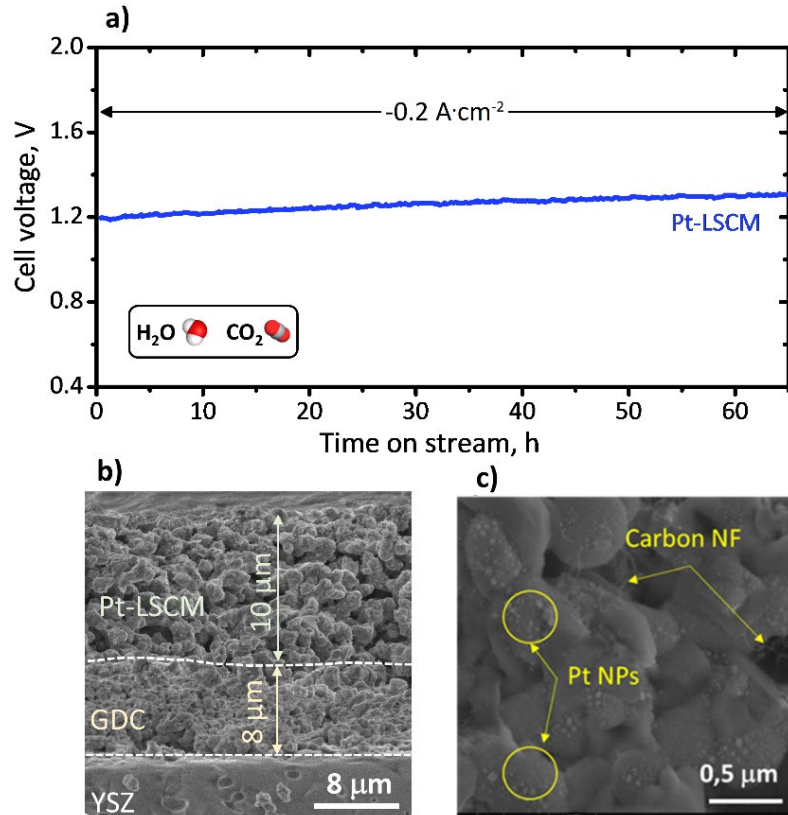


**Figure 7:** a) Durability study of the Pt/LSCrM electrode for 65 h in co-electrolysis mode in the absence of  $\text{H}_2$  feed. Reaction condition 25% $\text{H}_2\text{O}$  - 25% $\text{CO}_2$  - 50% He, at  $I = -0.2 \text{ A}\cdot\text{cm}^{-2}$ . SEM micrographs of Pt/LSCrM after stability test b) cross-section c) surface morphology.

## CONCLUSIONS

ALD of Pt has been applied for boosting the performance of LSCrM cathodes during CO<sub>2</sub> and H<sub>2</sub>O co-electrolysis in SOECs. The ALD process used was able to introduce dispersed Pt nanoparticles (18 nm average size upon heat exposure) at low loadings ( $51 \pm 2 \mu\text{g}\cdot\text{cm}^{-2}$ ) into the open volume of the LSCrM perovskite electrode. The electrochemical characterizations showed that the deposition of Pt significantly decreases the LSCrM's polarization resistance, as a result of improved electrocatalytic activity and electrical conductivity. In particular the rate of syngas production is improved up to 62% (at 1.5V, 850 °C) vs the bare LSCrM electrode during electrolysis operation, whereas the peak power output was enhanced by up to 84% in fuel cell mode. The results obtained here clearly show the advantage of using Pt ALD on redox stable perovskite material for efficient production of syngas at the adjustable ratio of H<sub>2</sub>/CO. The Pt/LSCrM cell displayed adequate durability during continuous operation for 60 h at 850 °C with marginal modifications in Pt particle size and population. The present results exemplify how ALD can provide an efficient route towards noble metal exploitation in solid oxide cells in order to transform renewable power into the raw material for chemical industry.

## SUPPORTING INFORMATION

XPS data of LSCrM prior and following Pt deposition with ALD, SEM images and XRD analysis of the examined cells, Analysis of the Pt nanoparticles size distribution, I-V curves obtained during steam, carbon dioxide and co-electrolysis with Pt-LSCrM sample.

## AUTHOR INFORMATION

### Corresponding authors

\*E-mail: [kyriakou@mit.edu](mailto:kyriakou@mit.edu), [M.Tsampas@diffier.nl](mailto:M.Tsampas@diffier.nl)

### ORCID

Vasileios Kyriakou: 0000-0002-7088-1160

Mihalis N. Tsampas: 0000-0002-4367-4457

## ACKNOWLEDGMENTS

This research was carried out within the SynCat@DIFFER program between the Dutch institute for fundamental energy research (DIFFER), Eindhoven university of Technology (TU/e) and Syngaschem BV and is funded jointly by the Netherlands Organization for Scientific Research (NWO) and Syngaschem BV. The authors would like also to acknowledge the TU/e-DIFFER impulse program for financial support and Patrick A. Hage for helping with the measurements of Pt loading.

## REFERENCES

- (1) Giménez-Gómez, J. M.; Teixidó-Figueras, J.; Vilella, C. The Global Carbon Budget: A Conflicting Claims Problem. *Clim. Change* **2016**. <https://doi.org/10.1007/s10584-016-1633-1>.
- (2) Gómez, S. Y.; Hotza, D. Current Developments in Reversible Solid Oxide Fuel Cells.

*Renewable and Sustainable Energy Reviews*. 2016.

<https://doi.org/10.1016/j.rser.2016.03.005>.

- (3) Ebbesen, S. D.; Jensen, S. H.; Hauch, A.; Mogensen, M. B. High Temperature Electrolysis in Alkaline Cells, Solid Proton Conducting Cells, and Solid Oxide Cells. *Chemical Reviews*. 2014. <https://doi.org/10.1021/cr5000865>.
- (4) Pandiyan, A.; Uthayakumar, A.; Subrayan, R.; Cha, S. W.; Krishna Moorthy, S. B. Review of Solid Oxide Electrolysis Cells: A Clean Energy Strategy for Hydrogen Generation. *Nanomater. Energy* **2019**. <https://doi.org/10.1680/jnaen.18.00009>.
- (5) Zheng, Y.; Wang, J.; Yu, B.; Zhang, W.; Chen, J.; Qiao, J.; Zhang, J. A Review of High Temperature Co-Electrolysis of H<sub>2</sub>O and CO<sub>2</sub> to Produce Sustainable Fuels Using Solid Oxide Electrolysis Cells (SOECs): Advanced Materials and Technology. *Chemical Society Reviews*. 2017. <https://doi.org/10.1039/c6cs00403b>.
- (6) Irvine, J. T. S.; Neagu, D.; Verbraeken, M. C.; Chatzichristodoulou, C.; Graves, C.; Mogensen, M. B. Evolution of the Electrochemical Interface in High-Temperature Fuel Cells and Electrolysers. *Nature Energy*. 2016. <https://doi.org/10.1038/nenergy.2015.14>.
- (7) Graves, C.; Ebbesen, S. D.; Jensen, S. H.; Simonsen, S. B.; Mogensen, M. B. Eliminating Degradation in Solid Oxide Electrochemical Cells by Reversible Operation. *Nat. Mater.* **2015**. <https://doi.org/10.1038/nmat4165>.
- (8) Mewafy, B.; Paloukis, F.; Papazisi, K. M.; Balomenou, S. P.; Luo, W.; Teschner, D.; Joubert, O.; Le Gal La Salle, A.; Niakolas, D. K.; Zafeiratos, S. Influence of Surface State on the Electrochemical Performance of Nickel-Based Cermet Electrodes during Steam Electrolysis. *ACS Appl. Energy Mater.* **2019**. <https://doi.org/10.1021/acsaem.9b00779>.

- (9) Hydrogen and Fuel Cells: Emerging Technologies and Applications. *Choice Rev. Online* **2006**. <https://doi.org/10.5860/choice.43-3411>.
- (10) Meng, J.; Yuan, N.; Liu, X.; Yao, C.; Liang, Q.; Zhou, D.; Meng, F.; Meng, J. Synergistic Effects of Intrinsic Cation Disorder and Electron-Deficient Substitution on Ion and Electron Conductivity in  $\text{La}_{1-x}\text{Sr}_x\text{Co}_{0.5}\text{Mn}_{0.5}\text{O}_{3-\delta}$  ( $x = 0, 0.5, \text{ and } 0.75$ ). *Inorg. Chem.* **2015**. <https://doi.org/10.1021/ic502989c>.
- (11) Bastidas, D. M.; Tao, S.; Irvine, J. T. S. A Symmetrical Solid Oxide Fuel Cell Demonstrating Redox Stable Perovskite Electrodes. *J. Mater. Chem.* **2006**. <https://doi.org/10.1039/b600532b>.
- (12) Sapountzi, F. M.; Brosda, S.; Papazisi, K. M.; Balomenou, S. P.; Tsiplakides, D. Electrochemical Performance of  $\text{La}_{0.75}\text{Sr}_{0.25}\text{Cr}_{0.9}\text{Mn}_{0.1}\text{O}_3$  Perovskites as SOFC Anodes in  $\text{CO}/\text{CO}_2$  Mixtures. *J. Appl. Electrochem.* **2012**. <https://doi.org/10.1007/s10800-012-0459-4>.
- (13) Papazisi, K. M.; Balomenou, S.; Tsiplakides, D. Synthesis and Characterization of  $\text{La}_{0.75}\text{Sr}_{0.25}\text{Cr}_{0.9}\text{Mn}_{0.1}\text{O}_3$  Perovskites as Anodes for CO-Fuelled Solid Oxide Fuel Cells. *J. Appl. Electrochem.* **2010**. <https://doi.org/10.1007/s10800-010-0150-6>.
- (14) Yan, J.; Chen, H.; Dogdibegovic, E.; Stevenson, J. W.; Cheng, M.; Zhou, X. D. High-Efficiency Intermediate Temperature Solid Oxide Electrolyzer Cells for the Conversion of Carbon Dioxide to Fuels. *J. Power Sources* **2014**. <https://doi.org/10.1016/j.jpowsour.2013.11.047>.
- (15) Wan, J.; Zhu, J. H.; Goodenough, J. B.  $\text{La}_{0.75}\text{Sr}_{0.25}\text{Cr}_{0.5}\text{Mn}_{0.5}\text{O}_{3-\delta} + \text{Cu}$  Composite Anode Running on  $\text{H}_2$  and  $\text{CH}_4$  Fuels. *Solid State Ionics* **2006**.

<https://doi.org/10.1016/j.ssi.2006.04.046>.

- (16) Tao, S.; Irvine, J. T. S. Synthesis and Characterization of  $(\text{La}_{0.75}\text{Sr}_{0.25})\text{Cr}_{0.5}\text{Mn}_{0.5}\text{O}_{3-\delta}$ , a Redox-Stable, Efficient Perovskite Anode for SOFCs. *J. Electrochem. Soc.* **2004**.  
<https://doi.org/10.1149/1.1639161>.
- (17) Zhang, X.; Song, Y.; Wang, G.; Bao, X. Co-Electrolysis of  $\text{CO}_2$  and  $\text{H}_2\text{O}$  in High-Temperature Solid Oxide Electrolysis Cells: Recent Advance in Cathodes. *Journal of Energy Chemistry*. 2017. <https://doi.org/10.1016/j.jechem.2017.07.003>.
- (18) Xing, R.; Wang, Y.; Zhu, Y.; Liu, S.; Jin, C. Co-Electrolysis of Steam and  $\text{CO}_2$  in a Solid Oxide Electrolysis Cell with  $\text{La}_{0.75}\text{Sr}_{0.25}\text{Cr}_{0.5}\text{Mn}_{0.5}\text{O}_{3-\delta}$ -Cu Ceramic Composite Electrode. *J. Power Sources* **2015**. <https://doi.org/10.1016/j.jpowsour.2014.10.066>.
- (19) Ruiz-Morales, J. C.; Canales-Vázquez, J.; Marrero-López, D.; Irvine, J. T. S.; Núñez, P. Improvement of the Electrochemical Properties of Novel Solid Oxide Fuel Cell Anodes,  $\text{La}_{0.75}\text{Sr}_{0.25}\text{Cr}_{0.5}\text{Mn}_{0.5}\text{O}_{3-\delta}$  and  $\text{La}_{4}\text{Sr}_{8}\text{Ti}_{11}\text{Mn}_{0.5}\text{Ga}_{0.5}\text{O}_{37.5-\delta}$ , Using Cu-YSZ-Based Cermets. *Electrochim. Acta* **2007**. <https://doi.org/10.1016/j.electacta.2007.05.060>.
- (20) Onn, T. M.; Küngas, R.; Fornasiero, P.; Huang, K.; Gorte, R. J. Atomic Layer Deposition on Porous Materials: Problems with Conventional Approaches to Catalyst and Fuel Cell Electrode Preparation. *Inorganics*. 2018. <https://doi.org/10.3390/inorganics6010034>.
- (21) Price, R.; Cassidy, M.; Grolig, J. G.; Mai, A.; Irvine, J. T. S. Preparation and Testing of Metal/ $\text{Ce}_{0.80}\text{Gd}_{0.20}\text{O}_{1.90}$  (Metal: Ni, Pd, Pt, Rh, Ru) Co-Impregnated  $\text{La}_{0.20}\text{Sr}_{0.25}\text{Ca}_{0.45}\text{TiO}_3$  Anode Microstructures for Solid Oxide Fuel Cells. *J. Electrochem. Soc.* **2019**. <https://doi.org/10.1149/2.1181904jes>.

- (22) Kyriakou, V.; Neagu, D.; Papaioannou, E. I.; Metcalfe, I. S.; van de Sanden, M. C. M.; Tsampas, M. N. Co-Electrolysis of H<sub>2</sub>O and CO<sub>2</sub> on Exsolved Ni Nanoparticles for Efficient Syngas Generation at Controllable H<sub>2</sub>/CO Ratios. *Appl. Catal. B Environ.* **2019**. <https://doi.org/10.1016/j.apcatb.2019.117950>.
- (23) Thommy, L.; Joubert, O.; Hamon, J.; Caldes, M. T. Impregnation versus Exsolution: Using Metal Catalysts to Improve Electrocatalytic Properties of LSCM-Based Anodes Operating at 600 °C. *Int. J. Hydrogen Energy* **2016**. <https://doi.org/10.1016/j.ijhydene.2016.06.088>.
- (24) Jardiel, T.; Caldes, M. T.; Moser, F.; Hamon, J.; Gauthier, G.; Joubert, O. New SOFC Electrode Materials: The Ni-Substituted LSCM-Based Compounds (La<sub>0.75</sub>Sr<sub>0.25</sub>)(Cr<sub>0.5</sub>Mn<sub>0.5</sub>-XNi<sub>x</sub>)O<sub>3-Δ</sub> and (La<sub>0.75</sub>Sr<sub>0.25</sub>)(Cr<sub>0.5</sub>-XNi<sub>x</sub>Mn<sub>0.5</sub>)O<sub>3-δ</sub>. *Solid State Ionics* **2010**. <https://doi.org/10.1016/j.ssi.2010.05.012>.
- (25) George, S. M. Atomic Layer Deposition: An Overview. *Chem. Rev.* **2010**. <https://doi.org/10.1021/cr900056b>.
- (26) Mackus, A. J. M.; Weber, M. J.; Thissen, N. F. W.; Garcia-Alonso, D.; Vervuurt, R. H. J.; Assali, S.; Bol, A. A.; Verheijen, M. A.; Kessels, W. M. M. Atomic Layer Deposition of Pd and Pt Nanoparticles for Catalysis: On the Mechanisms of Nanoparticle Formation. *Nanotechnology* **2015**. <https://doi.org/10.1088/0957-4484/27/3/034001>.
- (27) Grillo, F.; Moulijn, J. A.; Kreutzer, M. T.; van Ommen, J. R. Nanoparticle Sintering in Atomic Layer Deposition of Supported Catalysts: Kinetic Modeling of the Size Distribution. *Catal. Today* **2018**. <https://doi.org/10.1016/j.cattod.2018.02.020>.
- (28) Song, Z.; Norouzi Banis, M.; Liu, H.; Zhang, L.; Zhao, Y.; Li, J.; Doyle-Davis, K.; Li, R.;

- Knights, S.; Ye, S.; et al. Ultralow Loading and High-Performing Pt Catalyst for a Polymer Electrolyte Membrane Fuel Cell Anode Achieved by Atomic Layer Deposition. *ACS Catal.* **2019**. <https://doi.org/10.1021/acscatal.8b04504>.
- (29) Dai, P.; Xie, J.; Mayer, M. T.; Yang, X.; Zhan, J.; Wang, D. Solar Hydrogen Generation by Silicon Nanowires Modified with Platinum Nanoparticle Catalysts by Atomic Layer Deposition. *Angew. Chemie - Int. Ed.* **2013**. <https://doi.org/10.1002/anie.201303813>.
- (30) Christensen, S. T.; Elam, J. W.; Rabuffetti, F. A.; Ma, Q.; Weigand, S. J.; Lee, B.; Seifert, S.; Stair, P. C.; Poeppelmeier, K. R.; Hersam, M. C.; et al. Controlled Growth of Platinum Nanoparticles on Strontium Titanate Nanocubes by Atomic Layer Deposition. *Small* **2009**. <https://doi.org/10.1002/smll.200801920>.
- (31) Hajar, Y.; Di Palma, V.; Kyriakou, V.; Verheijen, M. A.; Baranova, E. A.; Vernoux, P.; Kessels, W. M. M.; Creatore, M.; van de Sanden, M. C. M.; Tsampas, M. Atomic Layer Deposition of Highly Dispersed Pt Nanoparticles on a High Surface Area Electrode Backbone for Electrochemical Promotion of Catalysis. *Electrochem. commun.* **2017**. <https://doi.org/10.1016/j.elecom.2017.09.023>.
- (32) Choi, H. J.; Bae, K.; Grieshammer, S.; Han, G. D.; Park, S. W.; Kim, J. W.; Jang, D. Y.; Koo, J.; Son, J. W.; Martin, M.; et al. Surface Tuning of Solid Oxide Fuel Cell Cathode by Atomic Layer Deposition. *Adv. Energy Mater.* **2018**. <https://doi.org/10.1002/aenm.201802506>.
- (33) Gong, Y.; Palacio, D.; Song, X.; Patel, R. L.; Liang, X.; Zhao, X.; Goodenough, J. B.; Huang, K. Stabilizing Nanostructured Solid Oxide Fuel Cell Cathode with Atomic Layer Deposition. *Nano Lett.* **2013**. <https://doi.org/10.1021/nl402138w>.

- (34) Cheng, Y.; Raman, A. S.; Paige, J.; Zhang, L.; Sun, D.; Chen, M. U.; Vojvodic, A.; Gorte, R. J.; Vohs, J. M. Enhancing Oxygen Exchange Activity by Tailoring Perovskite Surfaces. *J. Phys. Chem. Lett.* **2019**. <https://doi.org/10.1021/acs.jpcclett.9b01235>.
- (35) Opitz, A. K.; Nenning, A.; Rameshan, C.; Kubicek, M.; Götsch, T.; Blume, R.; Hävecker, M.; Knop-Gericke, A.; Rupprechter, G.; Klötzer, B.; et al. Surface Chemistry of Perovskite-Type Electrodes during High Temperature CO<sub>2</sub> Electrolysis Investigated by Operando Photoelectron Spectroscopy. *ACS Appl. Mater. Interfaces* **2017**. <https://doi.org/10.1021/acsami.7b10673>.
- (36) Kattel, S.; Liu, P.; Chen, J. G. Tuning Selectivity of CO<sub>2</sub> Hydrogenation Reactions at the Metal/Oxide Interface. *Journal of the American Chemical Society*. 2017. <https://doi.org/10.1021/jacs.7b05362>.
- (37) Porosoff, M. D.; Yan, B.; Chen, J. G. Catalytic Reduction of CO<sub>2</sub> by H<sub>2</sub> for Synthesis of CO, Methanol and Hydrocarbons: Challenges and Opportunities. *Energy and Environmental Science*. 2016. <https://doi.org/10.1039/c5ee02657a>.
- (38) Oshima, K.; Shinagawa, T.; Nogami, Y.; Manabe, R.; Ogo, S.; Sekine, Y. Low Temperature Catalytic Reverse Water Gas Shift Reaction Assisted by an Electric Field. In *Catalysis Today*; 2014. <https://doi.org/10.1016/j.cattod.2013.11.035>.
- (39) Goguet, A.; Meunier, F.; Breen, J. P.; Burch, R.; Petch, M. I.; Faur Ghenciu, A. Study of the Origin of the Deactivation of a Pt/CeO<sub>2</sub> Catalyst during Reverse Water Gas Shift (RWGS) Reaction. *J. Catal.* **2004**. <https://doi.org/10.1016/j.jcat.2004.06.011>.
- (40) Knoops, H. C. M.; MacKus, A. J. M.; Donders, M. E.; Van De Sanden, M. C. M.; Notten, P. H. L.; Kessels, W. M. M. Remote Plasma ALD of Platinum and Platinum Oxide Films.

- Electrochem. Solid-State Lett.* **2009**. <https://doi.org/10.1149/1.3125876>.
- (41) Heil, S. B. S.; Langereis, E.; Roozeboom, F.; Van De Sanden, M. C. M.; Kessels, W. M. M. Low-Temperature Deposition of TiN by Plasma-Assisted Atomic Layer Deposition. *J. Electrochem. Soc.* **2006**. <https://doi.org/10.1149/1.2344843>.
- (42) Aaltonen, T.; Ritala, M.; Sajavaara, T.; Keinonen, J.; Leskelä, M. Atomic Layer Deposition of Platinum Thin Films. *Chem. Mater.* **2003**. <https://doi.org/10.1021/cm021333t>.
- (43) Baker, L.; Cavanagh, A. S.; Seghete, D.; George, S. M.; MacKus, A. J. M.; Kessels, W. M. M.; Liu, Z. Y.; Wagner, F. T. Nucleation and Growth of Pt Atomic Layer Deposition on Al<sub>2</sub>O<sub>3</sub> Substrates Using (Methylcyclopentadienyl)-Trimethyl Platinum and O<sub>2</sub> Plasma. *J. Appl. Phys.* **2011**. <https://doi.org/10.1063/1.3555091>.
- (44) Futamura, S.; Muramoto, A.; Tachikawa, Y.; Matsuda, J.; Lyth, S. M.; Shiratori, Y.; Taniguchi, S.; Sasaki, K. SOFC Anodes Impregnated with Noble Metal Catalyst Nanoparticles for High Fuel Utilization. *Int. J. Hydrogen Energy* **2019**. <https://doi.org/10.1016/j.ijhydene.2019.01.223>.
- (45) Jiang, S. P.; Ye, Y.; He, T.; Ho, S. B. Nanostructured Palladium-La<sub>0.75</sub>Sr<sub>0.25</sub>Cr<sub>0.5</sub>Mn<sub>0.5</sub>O<sub>3</sub>/Y<sub>2</sub>O<sub>3</sub>-ZrO<sub>2</sub> Composite Anodes for Direct Methane and Ethanol Solid Oxide Fuel Cells. *J. Power Sources* **2008**. <https://doi.org/10.1016/j.jpowsour.2008.06.099>.
- (46) Grillo, F.; Van Bui, H.; Moulign, J. A.; Kreutzer, M. T.; Van Ommen, J. R. Understanding and Controlling the Aggregative Growth of Platinum Nanoparticles in Atomic Layer Deposition: An Avenue to Size Selection. *J. Phys. Chem. Lett.* **2017**.

<https://doi.org/10.1021/acs.jpcllett.6b02978>.

- (47) Ebbesen, S. D.; Knibbe, R.; Mogensen, M. Co-Electrolysis of Steam and Carbon Dioxide in Solid Oxide Cells. *J. Electrochem. Soc.* **2012**. <https://doi.org/10.1149/2.076208jes>.
- (48) Foit, S. R.; Vinke, I. C.; de Haart, L. G. J.; Eichel, R. A. Power-to-Syngas: An Enabling Technology for the Transition of the Energy System? *Angewandte Chemie - International Edition*. 2017. <https://doi.org/10.1002/anie.201607552>.
- (49) Mahmood, A.; Bano, S.; Yu, J. H.; Lee, K. H. Effect of Operating Conditions on the Performance of Solid Electrolyte Membrane Reactor for Steam and CO<sub>2</sub> Electrolysis. *J. Memb. Sci.* **2015**. <https://doi.org/10.1016/j.memsci.2014.09.002>.
- (50) Wang, Y.; Liu, T.; Lei, L.; Chen, F. High Temperature Solid Oxide H<sub>2</sub>O/CO<sub>2</sub> Co-Electrolysis for Syngas Production. *Fuel Processing Technology*. 2017. <https://doi.org/10.1016/j.fuproc.2016.08.009>.
- (51) Cao, Y.; Gao, Z.; Jin, J.; Zhou, H.; Cohron, M.; Zhao, H.; Liu, H.; Pan, W. Synthesis Gas Production with an Adjustable H<sub>2</sub>/CO Ratio through the Coal Gasification Process: Effects of Coal Ranks and Methane Addition. *Energy and Fuels* **2008**. <https://doi.org/10.1021/ef7005707>.
- (52) Tao, Y.; Ebbesen, S. D.; Mogensen, M. B. Carbon Deposition in Solid Oxide Cells during Co-Electrolysis of H<sub>2</sub>O and CO<sub>2</sub>. *J. Electrochem. Soc.* **2014**. <https://doi.org/10.1149/2.079403jes>.
- (53) Chen, K.; Jiang, S. P. Review - Materials Degradation of Solid Oxide Electrolysis Cells. *Journal of the Electrochemical Society*. 2016. <https://doi.org/10.1149/2.0101611jes>.

